Chemical Science

ROYAL SOCIETY OF CHEMISTRY

EDGE ARTICLE

View Article Online
View Journal | View Issue

Cite this: *Chem. Sci.*, 2025, **16**, 17232

All publication charges for this article have been paid for by the Royal Society of Chemistry

Received 29th June 2025
Accepted 17th August 2025

DOI: 10.1039/d5sc04788a

rsc.li/chemical-science

A natural ultrasound-triggered nitric oxide booster for endothelial dysfunction therapy

Yuqiong Wang,[a] Dong Meng,[c] Yu Dong,[a] Xiaoqing Huang,[a] Liping Wang,*[a] Wen Gao*[a] and Bo Tang [ab]

Vascular endothelial dysfunction constitutes a pivotal initiating event in atherosclerosis (AS) pathogenesis, characterized by upregulated inflammatory factors, elevated reactive oxygen species (ROS) production, and excessive nitric oxide (NO) depletion. The exogenous delivery of NO, while minimizing adverse effects on the human body, presents a potent strategy for maintaining vascular homeostasis during pathological events. Herein, a natural ultrasound (US)-triggered and "on-demand" NO booster (FPG) is constructed using *S*-nitrosoglutathione (GSNO) as the NO donor and fucoidan for its anti-inflammatory and antioxidant properties. RNA sequencing and western blot analyses reveal that US-activated FPG modulates nuclear factor erythroid-2-related factor 2 (Nrf2), nuclear factor kappa-B (NF-κB), and vascular endothelial growth factor (VEGF)/endothelial NO synthase (eNOS) pathways in oxidized low-density lipoprotein (ox-LDL)-stimulated human umbilical vein endothelial cells (HUVECs). This modulation attenuates oxidative stress, suppresses inflammatory responses, and enhances angiogenesis. Furthermore, US and histopathological imaging examinations indicate that combined FPG–US therapy reduces plaque area (% plaque area/tissue area: 0.10 ± 0.04%; $P = 0.003$ *vs.* high-fat diet group (2.25 ± 0.10%)) and preserves vascular integrity in high-fat diet mice. Collectively, this natural US-responsive NO booster establishes a robust foundation for developing targeted therapies against endothelial dysfunction and advancing innovative pharmacotherapeutic strategies for cardiovascular diseases.

Introduction

Atherosclerosis (AS), a chronic inflammatory disease of the arteries, is a leading global cause of cardiovascular events and strokes, posing significant threats to public health.[1–6] Endothelial dysfunction triggered by oxidized low-density lipoprotein (ox-LDL) is widely regarded as one of the earliest hallmarks of AS pathogenesis.[7–9] Mechanistically, ox-LDL binding to the lectin-like endothelial ox-LDL receptor (LOX-1) induces endothelial nitric oxide synthase (eNOS) uncoupling, thereby reducing nitric oxide (NO) production.[10–14] Concurrently, ox-LDL activates NADPH oxidases on the cell membrane to enhance the production of intracellular superoxide anion ($O_2^{\bullet-}$), which rapidly reacts with endogenous NO, leading to increased consumption of NO.[10,15–18] In response to this reduced NO availability, phenotypic transformation of endothelial cells (ECs) from a resting phenotype into a proatherogenic phenotype, which commonly is described as the starting point of AS and introduces excessive oxidative system activation, pro-inflammatory responding, and foam cell formation.[19–22] Given the critical role of NO in preserving and restoring endothelial integrity within vascular systems, targeted delivery of exogenous NO to atherosclerotic lesions has emerged as a promising therapeutic strategy to counteract early-stage AS.

At present, numerous strategies are being explored to improve the bioavailability of NO for the treatment of AS. Statins, clinically proven to mitigate AS risk by inducing vasodilation, exerting anti-inflammatory and antioxidant effects, and augmenting NO bioavailability,[23–27] are limited by adverse effects such as hepatotoxicity, nephrotoxicity, and hyperglycemia during prolonged use.[28–30] Consequently, diverse materials with therapeutic potential have been developed, albeit with mixed success. For instance, NO-releasing vascular stents and three-dimensional (3D) printed grafts effectively inhibited thrombosis and smooth muscle cell (SMC) proliferation while promoting endothelialization, yet they risk causing localized endothelial dysfunction near implantation sites.[31,32] The 3D biomimetic AS model based on hydrogel revealed that zinc ions influence AS progression through a concentration-dependent biphasic effect, but their therapeutic efficacy *in vivo* has not yet been fully validated.[33] Similarly, biodegradable polymer nanoparticles (NPs) demonstrated NO-driven angiogenesis in human

[a]*College of Chemistry, Chemical Engineering and Materials Science, Key Laboratory of Molecular and Nano Probes, Ministry of Education, Collaborative Innovation Center of Functionalized Probes for Chemical Imaging in Universities of Shandong, Institutes of Biomedical Sciences, Shandong Normal University, Jinan 250014, Shandong, China. E-mail: gaowen@sdnu.edu.cn; lipingwang@sdnu.edu.cn*

[b]*Laoshan Laboratory, Qingdao 266237, Shandong, China*

[c]*Department of Ultrasound, Qilu Hospital of Shandong University, Jinan 250012, Shandong, China*

umbilical vein endothelial cells (HUVECs) *in vitro*, but their efficacy is hampered by poor targeting and uncontrolled release.[34] To address these limitations, exogenous stimuli-responsive NO delivery systems have emerged as promising alternatives. A photo-responsive, platelet-mimicking NO nanoprodrug system has been developed to improve the inflammatory response within the lesion and promote endothelial cell migration.[35] Nevertheless, the unavoidable absorption and scattering of light present certain limitations.[36–38] In addition, a US-responsive nanoplatform designed for the co-delivery of NO and carbon monoxide (CO) has been engineered to enable synergistic sono-gaso-therapy against cancer; however, its long-term biosafety profile remains to be validated.[39] To successfully achieve spatial, temporal, or dose-controlled intelligent release mechanisms, an ideal NO booster must be tailored to exhibit the following characteristics: (1) superior biocompatibility; (2) exceptional targeting precision and the capability to release NO "on-demand" at the lesion site; and (3) the ability to penetrate deeply into tissue.

In this study, we developed a natural US-triggered NO booster, designated as FPG, which exhibits excellent biocompatibility. The system was synthesized *via* self-assembly of the NO donor *S*-nitrosoglutathione (GSNO), fucoidan (selected for its anti-inflammatory, antioxidant, and vascular endothelium-targeting properties), and amine–polyethylene glycol–amine (NH_2–PEG_{2000}–NH_2). US exposure facilitated the cleavage of GSNO and enabled the controlled release of NO. The therapeutic effects were elucidated through RNA sequencing, which revealed that following US irradiation, FPG mitigated oxidative stress and inflammatory responses induced by ox-LDL through regulation of the nuclear factor erythroid-2 related factor 2 (Nrf2) and nuclear factor kappa-B (NF-κB) pathways. Concurrently, FPG promoted angiogenesis by activating the vascular endothelial growth factor (VEGF)/eNOS signaling pathway. Following intravenous (i.v.) administration in high-fat diet (HFD)-fed apolipoprotein E-deficient ($ApoE^{-/-}$) mice, FPG selectively accumulated in atherosclerotic lesions and released NO *in situ* upon US exposure. After 8 weeks of US-guided therapy, the aortic arch plaque area (% plaque area/tissue area) in the HFD + FPG + US group ($0.10 \pm 0.04\%$; $P = 0.66$ *vs.* normal diet (ND) group) was not significantly different from that in the ND group. This intervention also inhibited vascular wall thickening and abnormal elevation in pulse wave velocity (PWV). Additionally, NO-driven angiogenesis improved aortic arch structural integrity and endothelial homeostasis. Critically, FPG outperformed the control drug atorvastatin (AT) in biosafety assessments. The FPG–US combinatorial platform represents a precise, on-demand NO delivery strategy with therapeutic potential for ameliorating endothelial dysfunction in AS.

Results and discussion

Synthesis and characterization of FPG

The US-triggered NO booster, FPG, was synthesized *via* the self-assembly of fucoidan, NH_2–PEG_{2000}–NH_2, and the NO donor GSNO. The synthetic schemes of FPG and FP are shown in Fig. 1a and S1, respectively. The schematic explicitly illustrates: (i) the electrostatic attraction between the negatively charged sulfate groups of fucoidan and the positively charged protonated amino groups of NH_2–PEG_{2000}–NH_2 under acidic conditions; (ii) the covalent coupling process, including EDC/NHS-mediated activation of the carboxyl groups of GSNO and subsequent amide bond formation with the amino groups of NH_2–PEG_{2000}–NH_2. Transmission electron microscopy (TEM) images revealed that both FPG and FP adopted spherical morphologies, with average diameters of 349.88 ± 15.12 nm and 346.22 ± 14.26 nm, respectively (Fig. 1b and S2a). Dynamic light scattering (DLS) analysis showed hydrodynamic diameters of 353.6 ± 1.8 nm for FPG and 347.7 ± 1.5 nm for FP, consistent with TEM measurements. Their polydispersity index (PDI) values (0.18 ± 0.02 and 0.23 ± 0.04, respectively) indicated excellent dispersibility (Fig. 1c and S2b). The zeta potentials of FPG and FP were less negative than that of free fucoidan, suggesting the possible occurrence of positive and negative charge interactions (Fig. 1d and S3). Characterization of FPG by Fourier transform infrared (FT-IR) spectra revealed absorption bands at 1160–1260 cm^{-1} (S=O), 843 cm^{-1} (C–O–S), 1475 cm^{-1} (N–H), 1520 cm^{-1} (N=O), and 1645–1720 cm^{-1} (C=O), which were respectively characteristic of the fucoidan, NH_2–PEG_{2000}–NH_2, and GSNO components (Fig. 1e).[40–43] Further validation *via* UV-vis spectroscopy identified the distinctive GSNO absorption peak at 335 nm in FPG (Fig. 1f),[40] with additional visual confirmation provided by the color similarity between FPG in PBS and free GSNO (Fig. S4). The GSNO loading efficiency in FPG was calculated to be 6.3%, and the encapsulation efficiency of GSNO was determined to be 56.7% according to the comparison of its concentrations before and after loading. The successfully synthesized FPG demonstrated favorable *in vitro* stability (Fig. S5), specifically degrading upon US stimulation and promoting the release of NO (Fig. S6). The release of NO could be precisely modulated by adjusting US power density, FPG concentration, or irradiation time (Fig. 1g and S7). The FTIR spectral analysis further revealed that the N=O peak at 1520 cm^{-1} gradually weakened with the prolongation of ultrasonic time, indicating the release of NO (Fig. S8). Notably, NO concentrations within the therapeutic range (10^{-12} to 10^{-7} M), which mediate vasodilation, angiogenesis, and cytoprotection,[44] were reliably achieved. Based on biosafety evaluations (Fig. S9), an optimized FPG concentration (0.6 mg mL^{-1}) and US power density (0.8 W cm^{-2}) were selected for subsequent cellular studies.

NO generation, anti-inflammatory, and antioxidation activities of FPG after US irradiation

HUVECs were treated with ox-LDL (50 μg mL^{-1}) for 24 h to construct dysfunctional endothelium cell models. Confocal fluorescence imaging and western blot analysis confirmed significant upregulation of P-selectin expression in ox-LDL-stimulated HUVECs (Fig. S10–S12). Imaging flow cytometry (IFC) further confirmed that FITC–FPG could efficiently bind to P-selectin on ox-LDL-induced HUVECs and gradually internalized into the interior of cells (Fig. S13). Leveraging this efficient cellular uptake, intracellular NO levels generated by US-

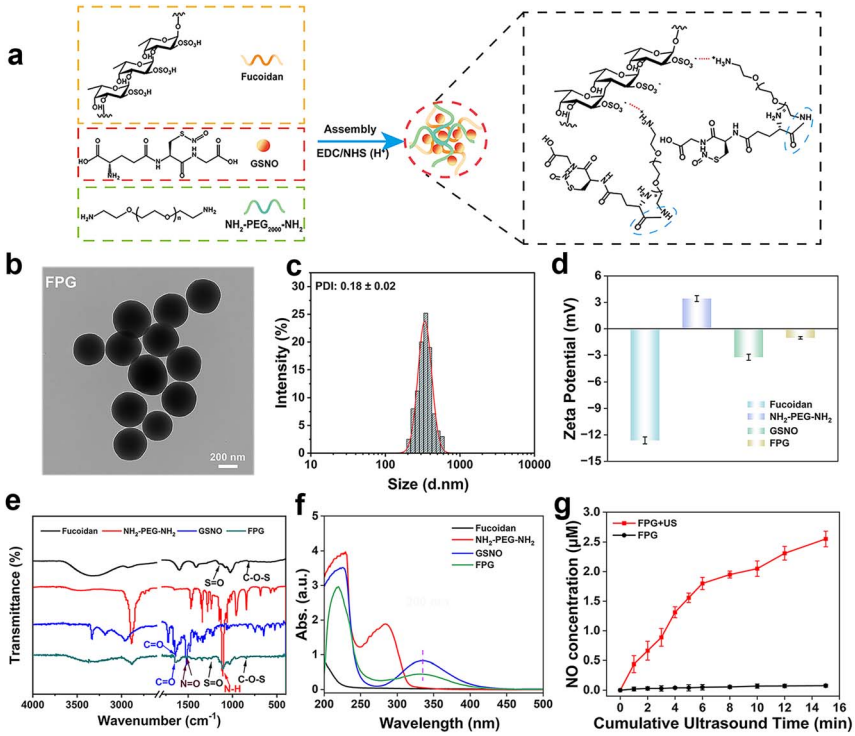

Fig. 1 Characterization of FPG. (a) Schematic illustration of the preparation of FPG. (b) Representative TEM image of FPG. Scale bar: 200 nm. (c) The size distribution and PDI of FPG in PBS. (d–f) Zeta potential, FTIR spectrum, and UV-vis absorption spectrum of fucoidan, NH_2–PEG_{2000}–NH_2, GSNO and FPG. (g) The NO release from FPG (0.6 mg mL^{-1}) under US irradiation at different accumulation times (0, 1, 2, 3, 4, 5, 6, 8, 10, 12, and 15 min). US parameters: 1.0 MHz, 50% duty cycle, 0.8 W cm^{-2}. Data are mean ± SD ($n = 3$).

activated FPG were quantified using the fluorescent probe DAF-FM DA. As depicted in Fig. 2a and b, intense green fluorescence was observed in the FPG + US group, which markedly diminished upon treatment with the NO scavenger carboxy-PTIO (cPTIO), confirming US-triggered NO release within cells.

Next, we evaluated whether FPG could attenuate inflammatory responses in ox-LDL-induced HUVECs by using ELISA. ox-LDL stimulation significantly increased secretion of pro-inflammatory cytokines, including interleukin-6 (IL-6), interleukin-1β (IL-1β), and tumor necrosis factor-α (TNF-α) (Fig. 2c–e). These elevations were substantially suppressed in HUVECs treated with FPG under US irradiation. Concurrently, ox-LDL induced excessive reactive oxygen species (ROS) production, particularly superoxide $O_2^{\bullet-}$.[45] The $O_2^{\bullet-}$ scavenging capacity of FPG was assessed using the fluorescent dye dihydroethidium (DHE), with fluorescence microscopy revealing that red fluorescence intensity was significantly reduced by 6.71-fold in the ox-LDL + FPG + US group compared to ox-LDL-treated cells (Fig. 2f and g). Given that $O_2^{\bullet-}$ reacts with NO to form cytotoxic peroxynitrite ($ONOO^-$), intracellular $ONOO^-$ levels were also measured.[46] It was discovered that the green fluorescence was scarcely detectable in HUVECs incubated with FPG after US irradiation. However, weak green fluorescence was seen in the ox-LDL and ox-LDL + US groups, which might be attributed to the existence of minor amounts of intracellular NO and $O_2^{\bullet-}$ reaction (Fig. S14). Taken together, these experiments disclose that FPG presents specific targeting ability against ox-LDL-induced HUVECs, with NO production as well as anti-inflammatory and antioxidant properties under US stimulation.

Proangiogenic capacity of FPG after US irradiation

NO is a critical regulator of angiogenesis and a pivotal mediator of cardiovascular homeostasis.[47] To evaluate the proangiogenic potential of the US-activated FPG system, we investigated its effects on HUVEC proliferation, migration, capillary-like tube formation, and CD31 expression. Scratch assay results revealed that the FPG + US group exhibited significantly reduced scratch width compared to FPG alone after 12 h and 24 h, as evidenced by qualitative imaging and quantitative analysis (Fig. S15). CCK-8 assay further confirmed that US-triggered FPG markedly enhanced HUVEC proliferation (Fig. S16). Next, the number of migrating ox-LDL-induced HUVECs in the FPG + US group was significantly greater than that in the FPG group, which was confirmed by the cell migration experiment (Fig. 3a and b). As the most direct evidence of angiogenesis, we further investigated the capacity of the FPG + US group to stimulate HUVEC tube formation through an *in vitro* tube formation assay. HUVECs were cultured in Matrigel and stained with calcein acetoxymethyl ester (calcein-AM) to visualize tube formation. In the absence of tubular organization, HUVECs tended to cluster together, forming large aggregates, consistent with previous findings.[48] Remarkably, the FPG + US group induced marked tubulogenesis, characterized by the assembly of elongated and interconnected HUVEC-formed tubules, compared to either the

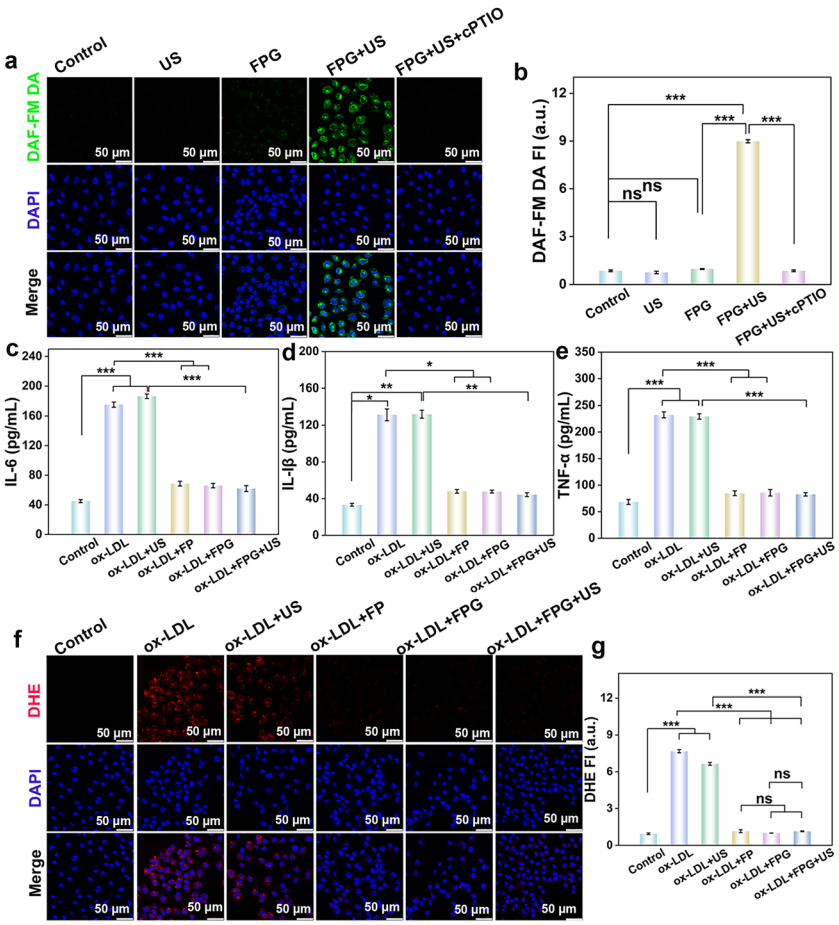

Fig. 2 *In vitro* NO generation, inflammation-attenuation and ROS-scavenging performance. (a) Representative confocal images of HUVECs after varied treatment, including US, FPG, FPG + US, and FPG + US + cPTIO. Cells incubated with medium alone served as the normal control. NO was stained by DAF-FM DA (green), and nuclei were stained with DAPI (blue). cPTIO (1 mM) was used as an NO scavenger. Scale bar: 50 μm. (b) Quantification of the fluorescence intensity of NO in (a). (c–e) Levels of inflammatory cytokines IL-6 (c), IL-1β (d), and TNF-α (e) secreted by HUVECs. (f) Fluorescence images showing intracellular $O_2^{\bullet-}$ levels after stimulation with ox-LDL and treatment with different formulations. Cells unstimulated with ox-LDL served as the normal control. $O_2^{\bullet-}$ was stained with DHE (red), and nuclei were stained with DAPI (blue). Scale bar: 50 μm. (g) Quantification of DHE fluorescence intensity. US parameters: 1.0 MHz, 50% duty cycle, 0.8 W cm^{-2} for 2 min. Data are mean ± SD ($n = 3$), * is $P < 0.05$, ** is $P < 0.01$, *** is $P < 0.001$, and ns is no significance by the one-way ANOVA test.

FPG group or the untreated control group (Fig. 3c). In addition, the quantitative analysis of the data further confirmed that the FPG + US group substantially promoted tubular formation of HUVECs, leading to a notable increase in the number of branching points, nodes, master junctions, and total branching length, in comparison with the FPG group (Fig. 3d–g). CD31 immunostaining corroborated these findings, with FPG + US displaying elevated fluorescence intensity, indicative of enhanced endothelial marker expression (Fig. 3h and i). Collectively, these data indicate that FPG + US robustly promotes endothelial tube formation exceptionally well.

Therapeutic mechanism of FPG after US irradiation

To elucidate the intrinsic mechanism of FPG-based nanotherapy in ox-LDL-treated HUVECs, RNA-sequencing (RNA-seq) analysis was subsequently performed. Three biological replicates in each group (ox-LDL 1–3 and ox-LDL + FPG + US 1–3) demonstrated a high degree of correlation (Fig. S17a). Principal component analysis (PCA) of transcriptomic data unveiled distinct profiles between the ox-LDL and ox-LDL + FPG + US groups (Fig. 4a). Concurrently, PCA performed on proteomic datasets not only exhibited tight clustering of biological replicates but also demonstrated clear discriminative separation between the two experimental groups (Fig. S18). We established a threshold of |log2 fold change (FC)| ≥ 1 and q-value ≤ 0.05 to filter out genes with significantly differential expression. The heat map revealed that a total of 714 mRNAs exhibited differential expression in biological effects following treatment with FPG under US irradiation (Fig. 4b). Volcano plot analysis further confirmed that, compared with the ox-LDL group, there were 327 up-regulated and 387 down-regulated mRNAs in the ox-LDL + FPG + US group (Fig. 4c and S17b). Notably, several significantly expressed genes associated with the regulation of inflammation, oxidative stress, and cell proliferation were labeled in the volcano plot, and these relevant genes were additionally visualized as a heatmap (Fig. 4d).

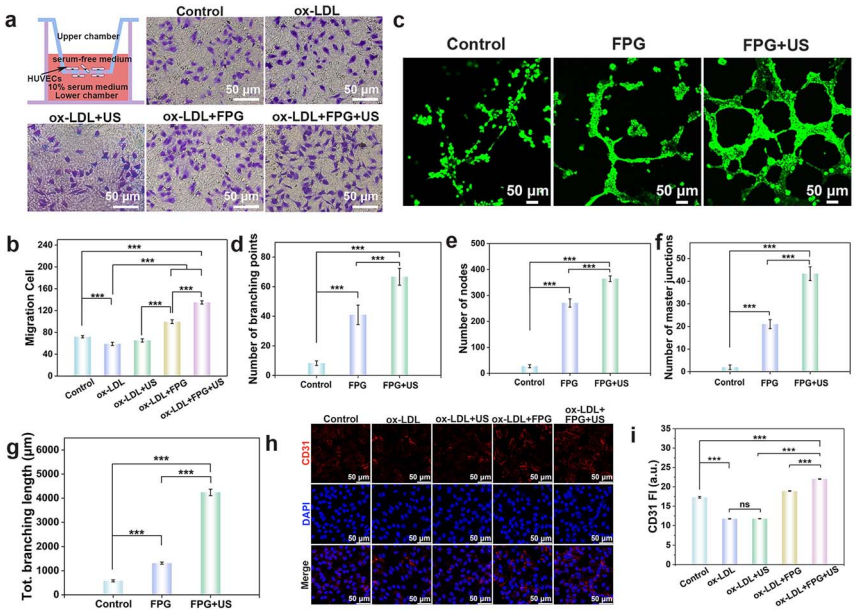

Fig. 3 *In vitro* angiogenesis of FPG under US irradiation. (a) A schematic illustration of the transwell migration assays and representative photomicrographs of HUVECs stained with crystal violet in transwell migration assays. Scale bar: 50 μm. (b) Quantification of migrated cells. (c) Tube formation of HUVECs treated with FPG under US irradiation. Scale bar: 50 μm. (d–g) Quantification of vascular progression ((d) number of branching points; (e) number of nodes; (f) number of master junctions; (g) total branching length) at 12 h. (h) Immunostaining photomicrographs of CD31 (red) and DAPI (blue). Scale bar: 50 μm. (i) Quantification of the immunostaining intensity of CD31. US parameters: 1.0 MHz, 50% duty cycle, 0.8 W cm^{-2} for 2 min. Data are mean ± SD ($n = 3$), *** is $P < 0.001$, and ns is no significance by the one-way ANOVA test.

Then, to obtain a superior comprehension of the biochemical pathways of differentially expressed genes (DEGs) induced by FPG + US, a bubble diagram of DEGs enriched in the Kyoto Encyclopedia of Genes and Genomes (KEGG) pathway was constructed. Notably, the TNF signaling pathway, VEGF signaling pathway, NF-κB signaling pathway, *etc.*, were implicated in the therapeutic process of FPG + US (Fig. 4e and S19). We further analyzed the expression of related proteins in the anti-inflammatory, antioxidant, and angiogenesis processes regulated by FPG + US through western blotting. The expression levels of Nrf2, VEGF, and P-eNOS were increased, while that of NF-κB was reduced in the HFD + FPG + US group (Fig. 4f, g, S20 and S21). Similar regulatory patterns of VEGF-mediated angiogenesis have been observed in other pathological contexts, such as hepatocellular carcinoma, where GP73-driven pro-angiogenic networks also involve VEGFA–VEGFR interactions to promote vascular endothelial cell activation.[49] Consistently, these results indicate that FPG exhibits significant anti-inflammatory effects, antioxidant responses, and angiogenesis capabilities in ox-LDL-induced HUVECs under US stimulation.

Therapeutic efficacy evaluation of FPG after US irradiation *in vivo*

Given the promising *in vitro* results, we further investigated the therapeutic efficacy of FPG combined with US in AS mice. $ApoE^{-/-}$ mice were randomized into seven groups: (1) normal diet (ND); (2) HFD; (3) HFD + US; (4) HFD + GSNO; (5) HFD + AT; (6) HFD + FPG; (7) HFD + FPG + US, and the corresponding formulations with 10 mg per kg FPG (0.63 mg per kg GSNO) and 10 mg kg^{-1} free AT were administered twice a week for a period of two months (Fig. 5a). We utilized echocardiography to measure the wall thickness and pulse wave velocity (PWV) of the aortic arch in real-time over a two-month treatment period as a novel diagnostic strategy for the detection of early AS. Since the mice were in the early stages of AS, there was no significant difference in the distance of the aortic arch as indicated by B-mode imaging among the groups (Fig. S22). Nonetheless, vascular wall thickness remained stable over time, reflecting the inherent structural stability of normal vasculature without pathological thickening in the ND group. Conversely, the HFD group exhibited a marked increase in vascular wall thickness, clearly demonstrating that a HFD regimen promotes vascular thickening ($P < 0.01$ *vs.* ND group). Among the intervention strategies, the HFD + FPG + US ($P > 0.05$ *vs.* ND group) combination elicited the smallest magnitude of wall thickening, which underscores the synergistic efficacy of FPG and US in mitigating pathological vascular structural changes (Fig. 5b and c). PWV, a gold-standard metric for arterial stiffness, was assessed *via* pulse-wave mode. Consistent with vascular wall thickness trends, PWV in the HFD group ($P < 0.05$ *vs.* ND group) increased sharply, indicative of exacerbated vascular stiffness. It is worth noting that the HFD + FPG + US ($P > 0.05$ *vs.* ND group; $P < 0.001$ *vs.* HFD group) intervention resulted in the smallest increase in PWV, highlighting its superior efficacy in maintaining vascular elasticity and functional integrity (Fig. 5d). Two months after the various treatments, the entire aortas and main organs from each group were collected for subsequent experiments. To evaluate the targeting specificity of FPG for HFD-induced vascular lesions, immunofluorescence staining was

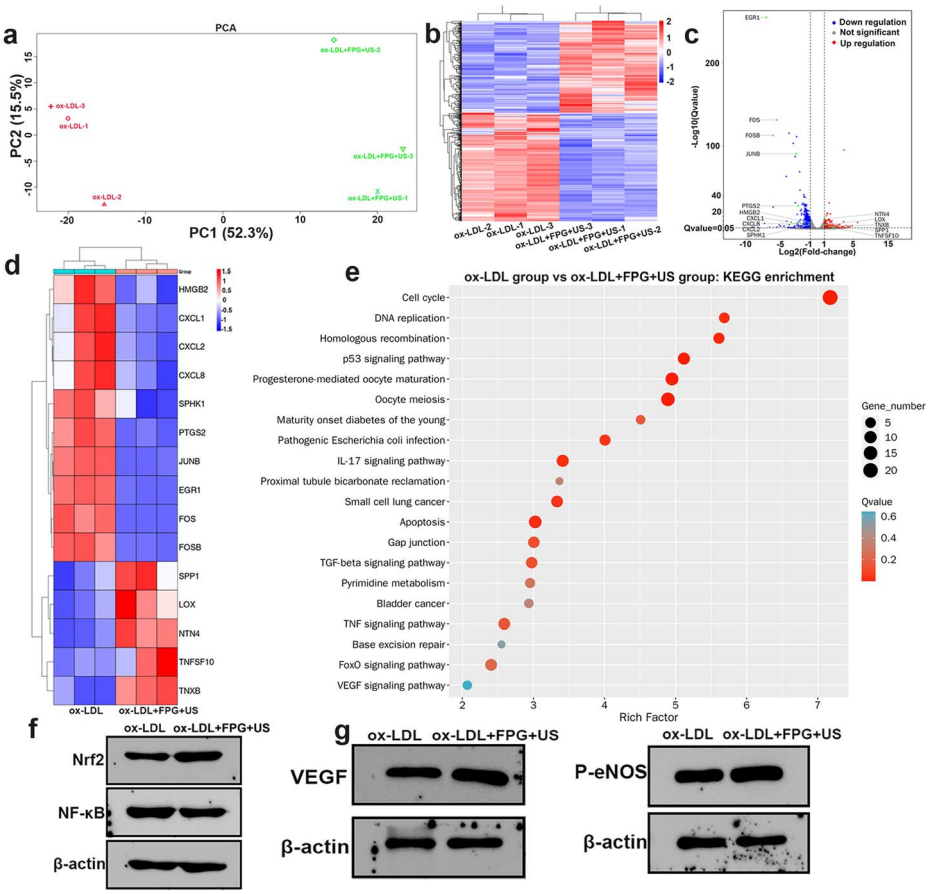

Fig. 4 Mechanism study of FPG under US irradiation for the treatment of dysfunctional endothelium cells by transcriptome high-throughput sequencing. (a) Principal component analysis (PCA) based on the DEGs from the ox-LDL and ox-LDL + FPG + US groups. (b) Heatmap of DEGs in the ox-LDL + FPG + US group compared with the ox-LDL group. (c) A comparison volcano map depicting upregulated (red) and downregulated (blue) genes through RNA-Seq analysis after FPG + US treatment on ox-LDL-induced HUVECs as compared to the ox-LDL group (DEGs; log2 FC ≥ 1 or ≤ -1, respectively, q-value ≤ 0.05). (d) Heatmap illustrating the relative changes in expression levels of selected genes in the ox-LDL + FPG + US group compared to the ox-LDL group. (e) The results of KEGG enrichment analysis from DEGs in the FPG + US group treated ox-LDL-induced HUVECs compared with the ox-LDL group. (f and g) Western blot analysis of Nrf2, NF-κB, VEGF, and P-eNOS. US parameters: 1.0 MHz, 50% duty cycle, 0.8 W cm^{-2} for 2 min. Data are mean ± SD ($n = 3$).

performed on aortic tissues. In the ND group, aortic sections showed minimal FITC–FPG fluorescence, indicating little non-specific binding under normal conditions. Conversely, sections from mice injected with FITC–FPG alone exhibited intense fluorescence throughout the aortic arch, demonstrating FPG's selective accumulation in HFD-induced lesions. To further verify the specificity of FPG accumulation, HFD mice were pre-treated with fucoidan prior to FPG injection, followed by aortic arch immunofluorescence staining. Notably, pre-treatment with fucoidan almost completely abolished the FITC–FPG signal. This suggests that fucoidan competes with FPG for binding sites, confirming the specificity of FPG accumulation in lesions (Fig. S23). Afterwards, the entire aortas were stained with Oil Red O (ORO) to quantitatively assess the lesion area on the intimal surface. Although plaque formation was not evident in the early stages of AS in mice, we could still conclude that the plaque area was distinctly reduced in the HFD + FPG + US group ($P < 0.001$ *vs.* HFD group), from 3.27 ± 0.15% to 0.99 ± 0.01% compared to the HFD group (Fig. 5e and S24). Consistent with these findings, ORO staining of aortic cross-sections demonstrated that the FPG + US treatment exhibited the most evident anti-AS efficacy among all treatments (Fig. 5f and S25). The plaque area in the HFD + FPG + US group (0.10 ± 0.04%, $P = 0.003$ *vs.* HFD group) was significantly smaller than that in the HFD group (2.25 ± 0.10%). Hematoxylin and eosin (H&E) staining highlighted severe vascular pathology in HFD mice, including vacuolization, disrupted elastic fibers, disorganized architecture, and wall thickening. In contrast, the ND and HFD + FPG + US groups exhibit intact endothelial layers with preserved structural integrity (Fig. 5g).

Subsequent analysis of NO levels in the aortic arch revealed comparable green fluorescence intensity between the HFD + FPG + US and ND groups, indicating restored NO bioavailability (Fig. S26a). Antioxidant activity assessments demonstrated minimal fluorescence signals in FPG-treated groups (FPG and FPG + US), with no detectable formation of highly toxic $ONOO^-$ (Fig. S26b and S27). After that, we found the lowest expression of IL-6, IL-1β, and TNF-α in serum from $ApoE^{-/-}$ mice that

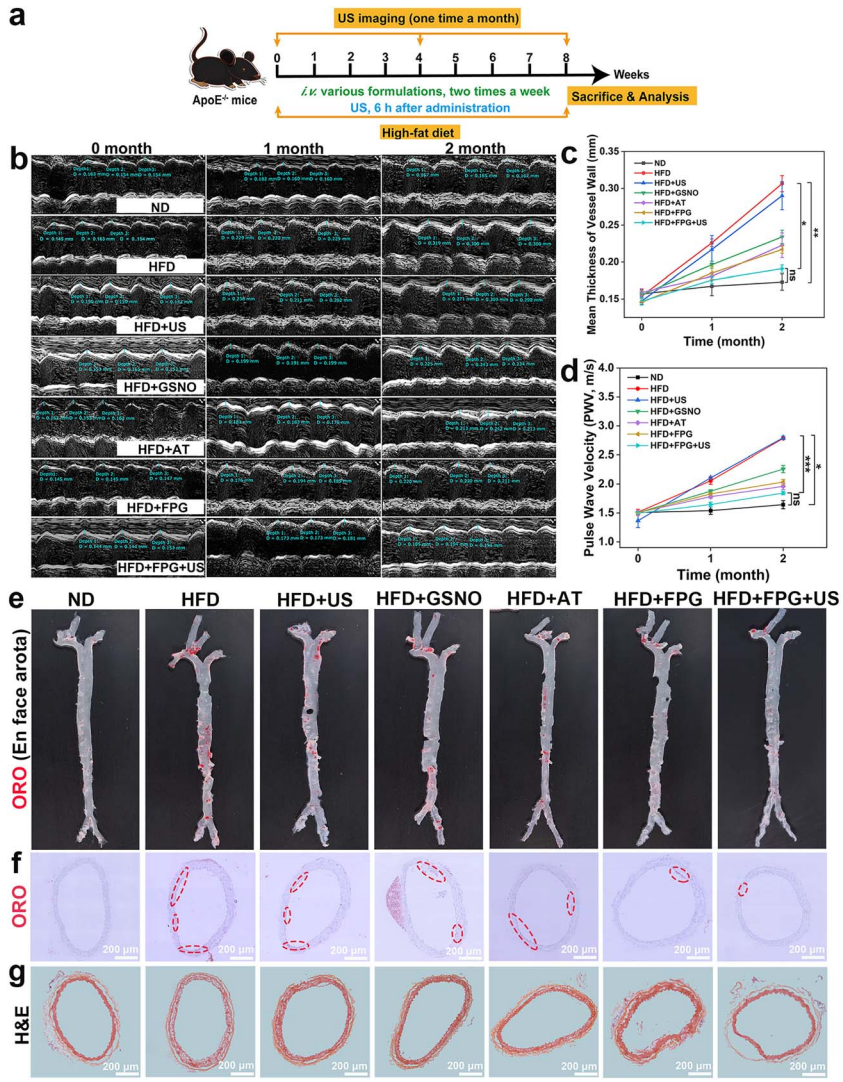

Fig. 5 Therapeutic effects of FPG with US irradiation in ApoE$^{-/-}$ mice. (a) Schematic diagram of the experimental design for anti-atherogenic therapy. (b) Representative M-mode of the aortic arch in ApoE$^{-/-}$ mice during treatment in different groups. (c) The mean thickness of blood vessel wall values in (b). (d) The PWV values of the aortic arch in ApoE$^{-/-}$ mice during treatment in different groups. (e) Representative *en face* images of ORO-stained aortas from each group of mice following different treatments. (f and g) Representative immunofluorescence micrographs of aortic arch sections stained with ORO (red areas represented lesions), H&E. Scale bar: 200 μm. US parameters: 1.0 MHz, 50% duty cycle, 0.8 W cm^{-2} for 2 min, 3 cycles. Data are mean ± SD ($n = 3$). * is $P < 0.05$, ** is $P < 0.01$, *** is $P < 0.001$, and ns is no significance by the one-way ANOVA test.

received FPG + US treatment (Fig. S28). Malondialdehyde (MDA), a lipid peroxidation product, serves as a widely recognized oxidative stress biomarker.[50] Glutathione (GSH) and superoxide dismutase (SOD) are key components of the antioxidant defense system against oxidative stress.[51,52] By analyzing serum levels of MDA, GSH, and SOD, we observed that the FPG + US group exhibited significantly lower MDA levels and higher GSH/SOD levels than the HFD group (Fig. S29). Furthermore, angiogenesis represents a critical indicator of tissue repair. Immunofluorescence staining for CD31 revealed a 1.76-fold increase in fluorescence intensity in the HFD + FPG + US group *versus* the HFD group, confirming the pro-angiogenic effect of FPG–US therapy (Fig. S30). We also measured the serum levels of Nrf2, NF-κB, VEGF, and P-eNOS, which are related to the regulation of anti-inflammatory, antioxidant, and angiogenesis processes. The results demonstrated that the levels of these markers in the HFD + FPG + US group were comparable to those in the ND group, indicating that FPG combined with US irradiation effectively alleviated atherosclerotic endothelial dysfunction (Fig. S31). Taken together, these findings establish that the anti-atherosclerotic efficacy of FPG + US arises from its ability to attenuate inflammation and oxidative stress while promoting endothelial repair at lesion sites, thereby achieving targeted and efficient AS therapy through a multifactorial mechanism.

Finally, we examined the potential adverse effects that may occur during and following a 2-month treatment with FPG under US excitation. During an 8-week observation period, the body weight of each mouse was recorded, and no obvious differences were observed in all seven groups (Fig. S32). Next,

hematological indicators, including red blood cells (RBC), white blood cells (WBC), platelets (PLT), and hemoglobin (HGB), were all within the normal range in each group. (Fig. S33). Also, biochemical markers related to liver (alanine aminotransferase, ALT, and aspartate aminotransferase, AST) and kidney (blood urea nitrogen, BUN, and serum creatinine, Scr) function in the HFD + FPG + US group were within the normal range. However, the levels of indicators of liver and kidney function in the HFD + AT group were slightly elevated (Fig. S34). The levels of total cholesterol (TC), low-density lipoprotein cholesterol (LDL-C), and triglycerides (TG) in the HFD + FPG + US group were significantly lower than in the ND group, whereas a marginal increase in high-density lipoprotein cholesterol (HDL-C) was noted (Fig. S35). Furthermore, H&E staining revealed no evident signs of tissue necrosis or morphological alterations in the organs across all groups (Fig. S36). Accordingly, all these findings indicate that i.v. administration of FPG is safe and causes no adverse effects on mice after US exposure.

Conclusions

In summary, we developed a multifunctional US-triggered NO booster through multicomponent self-assembly for targeted treatment of early-stage AS. FPG could actively recognize P-selectin, which was highly expressed by dysfunctional HUVECs. FPG, triggered by US, inherited the repair capacity of NO, as well as the broad-spectrum anti-inflammatory and antioxidant activity of fucoidan. The therapeutic effects were verified through RNA sequencing analysis, and the results showed that under ultrasonic stimulation, FPG alleviated oxidative stress and inflammatory responses induced by ox-LDL *via* modulation of the Nrf2 and NF-κB pathways, thereby reducing $O_2^{\bullet-}$, IL-6, IL-1β, and TNF-α. Additionally, FPG enhanced angiogenesis through the activation of the VEGF/eNOS signaling pathway. By targeting P-selectin, i.v.-administered FPG could be aggregated in areas of atherosclerotic plaques. Post-intravenous administration, the synergistic effect of FPG and US was found to effectively retard the progression of atherosclerosis in $ApoE^{-/-}$ mice. Notably, after 8 weeks of treatment under US image guidance, the HFD + FPG + US group did not display significant lipid accumulation or plaque formation in the aortic arch, preventing thickening of the vessel wall and an increase in PWV, in comparison to the other control therapy groups. Critically, FPG demonstrated superior biosafety compared to AT, with no systemic toxicity observed during prolonged intravenous use. Conclusively, the combination of FPG and US significantly decreases inflammation and oxidative stress levels and promotes angiogenesis, presenting a safe and effective NO-based approach for managing endothelial dysfunction.

Ethical statement

All animal experimental procedures were conducted in strict compliance with the relevant guidelines and ethical norms, which had been approved. All animal experiments were approved by the Institutional Animal Care and Use Committee of Shandong Normal University (approval no. AEECSDNU2024119) and conducted in accordance with relevant guidelines and regulations.

Author contributions

Yuqiong Wang and Wen Gao: conceptualization, validation, methodology, investigation, writing-original draft. Dong Meng, Yu Dong and Xiaoqing Huang: methodology, validation, investigation, writing-review & editing. Wen Gao and Liping Wang: supervision, writing-review & editing. Bo Tang, Wen Gao and Liping Wang: conceptualization, supervision, writing review & editing, funding acquisition.

Conflicts of interest

There are no conflicts to declare.

Data availability

All relevant data that support the findings of this study are available from the corresponding author upon reasonable request.

RNA sequencing raw data generated in this study have been deposited at the Sequence Read Archive database in NCBI under accession PRJNA1299778.

Data supporting this article have been included as part of the SI. The uncropped western blot images are specifically provided in Section 3 of the SI. See DOI: **https://doi.org/10.1039/d5sc04788a**.

Acknowledgements

This work was supported by the National Natural Science Foundation of China (22376128), the Major Science and Technology Innovation Project of Shandong Province (2021ZDSYS09), the Project of Shandong Provincial Center for Fundamental Science Research (YDZX2024150), and the Analysis and Test Center of College of Chemistry, Chemical Engineering and Materials Science, Shandong Normal University.

Notes and references

1 X. Duan, X. Yang, N. Mou, Y. Cao, Z. He, L. Zhu, Y. Zhong, K. Zhang, K. Qu, X. Qin, Q. Chen, Y. Luo and W. Wu, *Adv. Funct. Mater.*, 2024, **34**, 2405629.
2 S. Zhang, Z. Li, Y. Zhang, J. Chen, Y. Li, F. Wu, W. Wang, Z. J. Cui and G. Chen, *Adv. Sci.*, 2021, **8**, 2003410.
3 J. Chen, X. Zhang, R. Millican, J. Sherwood, S. Martin, H. Jo, Y. Yoon, B. C. Brott and H. Jun, *Adv. Drug Deliv. Rev.*, 2021, **170**, 142–199.
4 A. Khan and K. A. M. Jandeleit-Dahm, *Nat. Rev. Cardiol.*, 2025, 1–15.
5 C. Weber and H. Noels, *Nat. Med.*, 2011, **17**, 1410–1422.
6 C. Hu, Z. Zhang, S. Sun, H. Liu, L. Yuan and X. Zhang, *Coord. Chem. Rev.*, 2024, **510**, 215850.
7 J. Zheng and C. Lu, *Front. Cell Dev. Biol.*, 2020, **8**, 600950.

8 I. Falih, M. A. H. Alobeady, S. Banoon and M. Saleh, *J. Chem. Health Risks*, 2021, **11**, 71–83.
9 H. Jiang, Y. Zhou, S. M. Nabavi, A. Sahebkar, P. J. Little, S. Xu, J. Weng and J. Ge, *Front. Cardiovasc. Med.*, 2022, **9**, 925923.
10 P. Marchio, S. Guerra-Ojeda, J. M. Vila, M. Aldasoro, V. M. Victor and M. D. Mauricio, *Oxid. Med. Cell. Longev.*, 2019, **2019**, 8563845.
11 X. Guo, Y. Guo, Z. Wang, B. Cao, C. Zheng, Z. Zeng and Y. Wei, *Oxid. Med. Cell. Longev.*, 2022, **2022**, 7541411.
12 T. Yuan, T. Yang, H. Chen, D. Fu, Y. Hu, J. Wang, Q. Yuan, H. Yu, W. Xu and X. Xie, *Redox Biol.*, 2019, **20**, 247–260.
13 U. Förstermann, N. Xia and H. Li, *Circ. Res.*, 2017, **120**, 713–735.
14 U. Förstermann and W. C. Sessa, *Eur. Heart J.*, 2012, **33**, 829.
15 R. Hu, C. Dai, C. Dong, L. Ding, H. Huang, Y. Chen and B. Zhang, *ACS Nano*, 2022, **16**, 15959–15976.
16 X. Chen, K. Xun, Q. Wu, T. Zhang, J. Shi and G. Du, *Vasc. Pharmacol.*, 2007, **47**, 1–9.
17 M. Munno, A. Mallia, A. Greco, G. Modafferi, C. Banfi and S. Eligini, *Antioxidants*, 2024, **13**, 583.
18 M. Batty, M. R. Bennett and E. Yu, *Cells*, 2022, **11**, 3843.
19 Z. Wu, M. Zhou, X. Tang, J. Zeng, Y. Li, Y. Sun, J. Huang, L. Chen, M. Wan and C. Mao, *ACS Nano*, 2022, **16**, 3808–3820.
20 L. Zhou, Z. Wang, L. Wang, X. Zhang and Y. Xiao, *J. Am. Chem. Soc.*, 2023, **145**, 28296–28306.
21 A. G. Herman and S. Moncada, *Eur. Heart J.*, 2005, **26**, 1945.
22 S. Wang, Y. Wang, X. Lai, J. Sun, M. Hu, M. Chen, C. Li, F. Xu, C. Fan, X. Liu, Y. Song, G. Chen and Y. Deng, *ACS Nano*, 2023, **17**, 2761–2781.
23 H. Kim, S. Kumar, D.-W. Kang, H. Jo and J.-H. Park, *ACS Nano*, 2020, **14**, 6519–6531.
24 L. M. Pham, E.-C. Kim, W. Ou, C. D. Phung, T. Nguyen, T. Pham, K. Poudel, M. Gautam, H. Nguyen, J.-H. Jeong, C. Yong, S.-Y. Park, J.-R. Kim and J. Kim, *Biomaterials*, 2021, **269**, 120677.
25 M. Jia, Q. Li, J. Guo, W. Shi, L. Zhu, Y. Huang, Y. Li, L. Wang, S. Ma, T. Zhuang, X. Wang, Q. Pan, X. Wei, Y. Qin, X. Li, J. Jin, Xi. Zhi, J. Tang, Q. Jing, S. Li, L. Jiang, L. Qu, E. Osto, J. Zhang, X. Wang, B. Yu and D. Meng, *Circ. Res.*, 2022, **130**, 1038–1055.
26 C. Gao, Q. Huang, C. Liu, C. H. T. Kwong, L. Yue, J.-B. Wan, S. M. Y. Lee and R. Wang, *Nat. Commun.*, 2020, **11**, 2622.
27 W. Chen, C. Chen, M. Hsu, R. Chang, T. Lee and C. Wang, *Biomed. Pharmacother.*, 2024, **171**, 116192.
28 S. Choi, J. Kim, Y. Park, D. Lee, M. Park, J. Yee, Y. Chang, T. Song and H. Gwak, *Cardiovasc. Drugs Ther.*, 2024, 1–10.
29 T. Huang, T. Wu, Y. Wu, X. Li, J. Tan, C. Shen, S. Xiong, Z. Feng, S. Gao, H. Li and W. Cai, *Nat. Commun.*, 2023, **14**, 390.
30 Y. Lin, S. Wang, Z. Li, Y. Zhou, R. Wang, Y. Wang and Y. Chen, *Adv. Sci.*, 2024, **11**, 2403451.
31 N. Lyu, Z. Du, H. Qiu, P. Gao, Q. Yao, K. Xiong, Q. Tu, X. Li, B. Chen, M. Wang, G. Pan, N. Huang and Z. Yang, *Adv. Sci.*, 2020, **7**, 2002330.
32 Y. Shen, J. Cui, X. Yu, J. Song, P. Cai, W. Guo, Y. Zhao, J. Wu, H. Gu, B. Sun and X. Mo, *Smart Mater. Med.*, 2024, **5**, 36–51.
33 Y. Wang, N. Huang and Z. Yang, *Adv. Sci.*, 2023, **10**, 2300475.
34 C. Yang, H. Hwang, S. Jeong, D. Seo, Y. Jeong, D. Lee and K. Lee, *Int. J. Nanomed.*, 2018, **13**, 6517.
35 Y. Chai, L. Shangguan, H. Yu, Y. Sun, X. Huang, Y. Zhu, H.-Y. Wang and Y. Liu, *Adv. Sci.*, 2024, **11**, 2304994.
36 L. Zong, R. Teng, H. Zhang, W. Liu, Y. Feng, Z. Lu, Y. Zhou, Z. Fan, M. Li and X. Pu, *Adv. Sci.*, 2024, **11**, 2406022.
37 Y. Wang, Q. Tang, R. Wu, S. Sun, J. Zhang, J. Chen, M. Gong, C. Chen and X. Liang, *ACS Nano*, 2023, **17**, 3557–3573.
38 M. Sun, T. Yue, C. Wang, Z. Fan, E. Gazit and J. Du, *ACS Nano*, 2022, **16**, 9183–9194.
39 Y. Opoku-Damoah, Z. P. Xu, H. T. Ta and R. Zhang, *ACS Appl. Bio Mater.*, 2024, **7**, 7585–7594.
40 J. An, Y.-G. Hu, C. Li, X.-L. Hou, K. Cheng, B. Zhang, R.-Y. Zhang, D.-Y. Li, S.-J. Liu, B. Liu, D. Zhu and Y.-D. Zhao, *Biomaterials*, 2020, **230**, 119636.
41 M. Liu, Y. Zhang, X. Ma, B. Zhang, Y. Huang, J. Zhao, S. Wang, Y. Li, Y. Zhu, J. Xiong, T. He, Y. Wang, W. Han, K. Yang, X. Bi, Y. Liu and H. Zhang, *Oxid. Med. Cell. Longevity*, 2022, **2022**, 8006642.
42 Z. Li, Z. Song, C. He, J. Fan, W. Yu, M. Yang, P. Li, R. Luo, J. Zhou, S. Xu, B. Liu and S. Cheng, *Mater. Today Adv.*, 2022, **16**, 100321.
43 K. K. Razmjooee, F. Oustadi, A. Golaghaei and E. Nassireslami, *Biomed. Mater.*, 2022, **17**, 1–26.
44 L. Xu, Y. Chen, Q. Jin, T. Gao, C. Deng, R. Wang, Y. Wang, Y. Bai, J. Xu, W. Wu, H. Li, L. Fang, J. Wang, Y. Yang, L. Zhang, Q. Lv and M. Xie, *Small Struct.*, 2023, **4**, 2300004.
45 M. Munno, A. Mallia, A. Greco, G. Modafferi, C. Banfi and S. Eligini, *Antioxidants*, 2024, **13**, 583.
46 L. Yang, D. Wang, H. Jia, C. Yang, Y. Zhang, H. Li, J. Liu and J. Liu, *Adv. Mater.*, 2023, **35**, 2301455.
47 H. G. Augustin and G. Y. Koh, *Cell*, 2024, **187**, 4833–4858.
48 L. Guo, Q. Yang, R. Wei, W. Zhang, N. Yin, Y. Chen, C. Xu, C. Li, R. P. Carney, Y. Li and M. Feng, *Nat. Commun.*, 2023, **14**, 7334.
49 J. Ye, X. Gao, X. Huang, S. Huang, D. Zeng, W. Luo, C. Zeng, C. Lu, L. Lu, H. Huang, K. Mo, J. Huang, S. Li, M. Tang, T. Wu, R. Mai, M. Luo, M. Xie, S. Wang, Y. Li, Y. Lin and R. Liang, *Research*, 2024, **7**, 0387.
50 Y. Ma, W. Sun, Z. Ye, L. Liu, M. Li, J. Shang, X. Xu, H. Cao, L. Xu, Y. Liu, X. Kong, G. Song and X.-B. Zhang, *Sci. Adv.*, 2023, **9**, eadh1037.
51 W. Liu, Y. Zhang, G. Wei, M. Zhang, T. Li, Q. Liu, Z. Zhou, Y. Du and H. Wei, *Angew. Chem., Int. Ed.*, 2023, **62**, e202304465.
52 D. Matuz-Mares, H. Riveros-Rosas, M. Vilchis-Landeros and H. Vazquez-Meza, *Antioxidants*, 2021, **10**, 1220.